Analysis of the chicken retina with an adaptive optics multiphoton microscope

Juan M. Bueno,[1,*] Anastasia Giakoumaki,[1] Emilio J. Gualda,[1] Frank Schaeffel,[2] and Pablo Artal[1]

[1]*Laboratorio de Óptica, Centro de Investigación en Óptica y Nanofísica, Universidad de Murcia, Campus de Espinardo (Edificio 34), 30100 Murcia, Spain*
[2]*Section of Neurobiology of the Eye, Ophthalmic Research Institute, Calwerstrasse 7/1, 72076 Tuebingen, Germany*
*bueno@um.es

Abstract: The structure and organization of the chicken retina has been investigated with an adaptive optics multiphoton imaging microscope in a backward configuration. Non-stained flat-mounted retinal tissues were imaged at different depths, from the retinal nerve fiber layer to the outer segment, by detecting the intrinsic nonlinear fluorescent signal. From the stacks of images corresponding to the different retinal layers, volume renderings of the entire retina were reconstructed. The density of photoreceptors and ganglion cells layer were directly estimated from the images as a function of the retinal eccentricity. The maximum anatomical resolving power at different retinal eccentricities was also calculated. This technique could be used for a better characterization of retinal alterations during myopia development, and may be useful for visualization of retinal pathologies and intoxication during pharmacological studies.

©2011 Optical Society of America

OCIS codes: (170.3880) Medical and biological imaging; (180.4315) Nonlinear microscopy; (010.1080) Adaptive optics; (170.4470) Ophthalmology

References and links

1. J. Wallman and J. Winawer, "Homeostasis of eye growth and the question of myopia," Neuron **43**(4), 447–468 (2004).
2. M. L. Kisilak, J. J. Hunter, L. Huang, M. C. W. Campbell, and E. L. Irving, "In chicks wearing high powered negative lenses, spherical refraction is compensated and oblique astigmatism is induced," J. Mod. Opt. **55**(4), 611–623 (2008).
3. J. J. Hunter, M. C. W. Campbell, M. L. Kisilak, and E. L. Irving, "Blur on the retina due to higher-order aberrations: comparison of eye growth models to experimental data," J. Vis. **9**(6), 12, 1–20 (2009).
4. F. Schaeffel, H. C. Howland, and L. Farkas, "Natural accommodation in the growing chicken," Vision Res. **26**(12), 1977–1993 (1986).
5. F. Schaeffel, A. Glasser, and H. C. Howland, "Accommodation, refractive error and eye growth in chickens," Vision Res. **28**(5), 639–657 (1988).
6. J. Wallman and J. I. Adams, "Developmental aspects of experimental myopia in chicks: susceptibility, recovery and relation to emmetropization," Vision Res. **27**(7), 1139–1163 (1987).
7. C. F. Wildsoet and J. D. Pettigrew, "Experimental myopia and anomalous eye growth-patterns unaffected by optic-nerve section in chickens: evidence for local-control of eye growth," Clin. Vis. Sci. **3**, 99–107 (1988).
8. J. G. Sivak, D. L. Barrie, and J. A. Weerheim, "Bilateral experimental myopia in chicks," Optom. Vis. Sci. **66**(12), 854–858 (1989).
9. G. Davis Buckner, R. H. Wilkins, and J. H. Kastle, "The normal growth of White Leghorn chickens," Am. J. Physiol. **47**, 393–398 (1918).
10. S. Mar, M. C. Martinez-Garcia, J. T. Blanco-Mezquita, R. M. Torres, and J. Merayo-Lloves, "Measurement of correlation between transmission and scattering during wound healing in hen corneas," J. Mod. Opt. **56**(8), 1014–1021 (2009).
11. M. C. Martínez-García, J. Merayo-Llovés, T. Blanco-Mezquita, and S. Mar-Sardaña, "Wound healing following refractive surgery in hens," Exp. Eye Res. **83**(4), 728–735 (2006).
12. R. M. Torres, J. Merayo-Lloves, J. T. Blanco-Mezquita, C. P. Günther, G. Rodríguez, R. Gutiérez, and C. Martínez-García, "Experimental model of laser in situ keratomileusis in hens," J. Refract. Surg. **21**(4), 392–398 (2005).
13. W. C. Fowler, D. H. Chang, B. C. Roberts, E. L. Zarovnaya, and A. D. Proia, "A new paradigm for corneal wound healing research: the white leghorn chicken (*Gallus gallus domesticus*)," Curr. Eye Res. **28**(4), 241–250 (2004).

1

14. R. L. Trelstad and A. J. Coulombre, "Morphogenesis of the collagenous stroma in the chick cornea," J. Cell Biol. **50**(3), 840–858 (1971).
15. C. Boote, S. Hayes, S. Jones, A. J. Quantock, P. M. Hocking, C. F. Inglehearn, M. Ali, and K. M. Meek, "Collagen organization in the chicken cornea and structural alterations in the retinopathy, globe enlarged (rge) phenotype--an X-ray diffraction study," J. Struct. Biol. **161**(1), 1–8 (2008).
16. C. J. Wolsley, K. J. Saunders, G. Silvestri, and R. S. Anderson, "Investigation of changes in the myopic retina using multifocal electroretinograms, optical coherence tomography and peripheral resolution acuity," Vision Res. **48**(14), 1554–1561 (2008).
17. S. Y. Kim, N. Ondhia, D. Vidgen, L. Malaval, M. Ringuette, and V. I. Kalnins, "Spatiotemporal distribution of SPARC/osteonectin in developing and mature chicken retina," Exp. Eye Res. **65**(5), 681–689 (1997).
18. W. Denk, J. H. Strickler, and W. W. Webb, "Two-photon laser scanning fluorescence microscopy," Science **248**(4951), 73–76 (1990).
19. Y. Guo, P. P. Ho, H. Savage, D. Harris, P. Sacks, S. Schantz, F. Liu, N. Zhadin, and R. R. Alfano, "Second-harmonic tomography of tissues," Opt. Lett. **22**(17), 1323–1325 (1997).
20. E. J. Gualda, J. M. Bueno, and P. Artal, "Wavefront optimized nonlinear microscopy of ex vivo human retinas," J. Biomed. Opt. **15**(2), 026007 (2010).
21. J. M. Bueno, E. J. Gualda, and P. Artal, "Analysis of corneal stroma organization with wavefront optimized nonlinear microscopy," Cornea **30**(6), 692–701 (2011).
22. J. M. Bueno, E. J. Gualda, and P. Artal, "Adaptive optics multiphoton microscopy to study ex vivo ocular tissues," J. Biomed. Opt. **15**(6), 066004 (2010).
23. F. Schaeffel and H. C. Howland, "Visual optics in normal and ametropic chickens," Clin. Vis. Sci. **3**, 83–89 (1988).
24. L. Reymond, "Spatial visual acuity of the eagle *Aquila audax*: a behavioural, optical and anatomical investigation," Vision Res. **25**(10), 1477–1491 (1985).
25. J. I. Yellott, Jr., "Spectral analysis of spatial sampling by photoreceptors: topological disorder prevents aliasing," Vision Res. **22**(9), 1205–1210 (1982).
26. N. J. Coletta and D. R. Williams, "Psychophysical estimate of extrafoveal cone spacing," J. Opt. Soc. Am. A **4**(8), 1503–1513 (1987).
27. P. Artal and R. Navarro, "High-resolution imaging of the living human fovea: measurement of the intercenter cone distance by speckle interferometry," Opt. Lett. **14**(20), 1098–1100 (1989).
28. M. Bartmann and F. Schaeffel, "A simple mechanism for emmetropization without cues from accommodation or colour," Vision Res. **34**(7), 873–876 (1994).
29. F. Schaeffel, B. Rohrer, E. Zrenner, and T. Lemmer, "Diurnal control of rod function in the chicken," Vis. Neurosci. **6**(06), 641–653 (1991).
30. N. S. Hart, T. J. Lisney, and S. P. Collin, "Cone photoreceptor oil droplet pigmentation is affected by ambient light intensity," J. Exp. Biol. **209**(23), 4776–4787 (2006).
31. M. J. Tovée, *An Introduction to the Visual System* (Cambridge University Press, 1996).
32. D. Schweitzer, S. Schenke, M. Hammer, F. Schweitzer, S. Jentsch, E. Birckner, W. Becker, and A. Bergmann, "Towards metabolic mapping of the human retina," Microsc. Res. Tech. **70**(5), 410–419 (2007).
33. C. H. Chen, E. Tsina, M. C. Cornwall, R. K. Crouch, S. Vijayaraghavan, and Y. Koutalos, "Reduction of all-trans retinal to all-trans retinol in the outer segments of frog and mouse rod photoreceptors," Biophys. J. **88**(3), 2278–2287 (2005).
34. S. H. Huang, A. A. Heikal, and W. W. Webb, "Two-photon fluorescence spectroscopy and microscopy of NAD(P)H and flavoprotein," Biophys. J. **82**(5), 2811–2825 (2002).
35. Y. Imanishi, M. L. Batten, D. W. Piston, W. Baehr, and K. Palczewski, "Noninvasive two-photon imaging reveals retinyl ester storage structures in the eye," J. Cell Biol. **164**(3), 373–383 (2004).
36. M. Han, A. Bindewald-Wittich, F. G. Holz, G. Giese, M. H. Niemz, S. Snyder, H. Sun, J. Y. Yu, M. Agopov, O. La Schiazza, and J. F. Bille, "Two-photon excited autofluorescence imaging of human retinal pigment epithelial cells," J. Biomed. Opt. **11**(1), 010501 (2006).
37. M. Han, G. Giese, S. Schmitz-Valckenberg, A. Bindewald-Wittich, F. G. Holz, J. Y. Yu, J. F. Bille, and M. H. Niemz, "Age-related structural abnormalities in the human retina-choroid complex revealed by two-photon excited autofluorescence imaging," J. Biomed. Opt. **12**(2), 024012 (2007).
38. J. J. Mancuso, A. M. Larson, T. G. Wensel, and P. Saggau, "Multiphoton adaptation of a commercial low-cost confocal microscope for live tissue imaging," J. Biomed. Opt. **14**(3), 034048 (2009).
39. B. G. Wang, A. Eitner, J. Lindenau, and K. J. Halbhuber, "High-resolution two-photon excitation microscopy of ocular tissues in porcine eye," Lasers Surg. Med. **40**(4), 247–256 (2008).
40. N. S. Hart, "The visual ecology of avian photoreceptors," Prog. Retin. Eye Res. **20**(5), 675–703 (2001).
41. M. S. Wai, D. E. Lorke, L. S. Kung, and D. T. Yew, "Morphogenesis of the different types of photoreceptors of the chicken (*Gallus domesticus*) retina and the effect of amblyopia in neonatal chicken," Microsc. Res. Tech. **69**(2), 99–107 (2006).
42. Y. A. Kram, S. Mantey, and J. C. Corbo, "Avian cone photoreceptors tile the retina as five independent, self-organizing mosaics," PLoS ONE **5**(2), e8992 (2010).
43. C. A. Curcio, K. R. Sloan, R. E. Kalina, and A. E. Hendrickson, "Human photoreceptor topography," J. Comp. Neurol. **292**(4), 497–523 (1990).
44. C. A. Curcio and K. R. Sloan, "Packing geometry of human cone photoreceptors: variation with eccentricity and evidence for local anisotropy," Vis. Neurosci. **9**(02), 169–180 (1992).

45. A. K. Goodchild, K. K. Ghosh, and P. R. Martin, "Comparison of photoreceptor spatial density and ganglion cell morphology in the retina of human, macaque monkey, cat, and the marmoset *Callithrix jacchus*," J. Comp. Neurol. **366**(1), 55–75 (1996).
46. L. Galli-Resta, E. Novelli, Z. Kryger, G. H. Jacobs, and B. E. Reese, "Modelling the mosaic organization of rod and cone photoreceptors with a minimal-spacing rule," Eur. J. Neurosci. **11**(4), 1461–1469 (1999).
47. M. J. Chandler, P. J. Smith, D. A. Samuelson, and E. O. MacKay, "Photoreceptor density of the domestic pig retina," Vet. Ophthalmol. **2**(3), 179–184 (1999).
48. M. L. Rahman, M. Aoyama, and S. Sugita, "Number and density of retinal photoreceptor cells with emphasis on oil droplet distribution in the Mallard Duck (*Anas platyrhynchos* var. *domesticus*)," J. Anim. Sci. **78**(6), 639–649 (2007).
49. M. L. Rahman, M. Aoyama, and S. Sugita, "Topography of retinal photoreceptor cells in the Jungle Crow (*Corvus macrorhynchos*) with emphasis on the distribution of oil droplets," Ornitholog. Sci. **6**(1), 29–38 (2007).
50. J. K. Bowmaker, "The visual pigments, oil droplets and spectral sensitivity of the pigeon," Vision Res. **17**(10), 1129–1138 (1977).
51. V. Porciatti, W. Hodos, G. Signorini, and F. Bramanti, "Electroretinographic changes in aged pigeons," Vision Res. **31**(4), 661–668 (1991).
52. M. M. Ghim and W. Hodos, "Spatial contrast sensitivity of birds," J. Comp. Physiol. A Neuroethol. Sens. Neural Behav. Physiol. **192**(5), 523–534 (2006).
53. E. Diedrich and F. Schaeffel, "Spatial resolution, contrast sensitivity, and sensitivity to defocus of chicken retinal ganglion cells in vitro," Vis. Neurosci. **26**(5-6), 467–476 (2009).
54. R. Over and D. Moore, "Spatial acuity of the chicken," Brain Res. **211**(2), 424–426 (1981).
55. K. L. Schmid and C. F. Wildsoet, "Assessment of visual acuity and contrast sensitivity in the chick using an optokinetic nystagmus paradigm," Vision Res. **38**(17), 2629–2634 (1998).
56. J. Naito and Y. Chen, "Morphological features of chick retinal ganglion cells," Anat. Sci. Int. **79**(4), 213–225 (2004).
57. D. Ehrlich, "Regional specialization of the chick retina as revealed by the size and density of neurons in the ganglion cell layer," J. Comp. Neurol. **195**(4), 643–657 (1981).
58. C. Straznicky and M. Chehade, "The formation of the area centralis of the retinal ganglion cell layer in the chick," Development **100**(3), 411–420 (1987).
59. Y. Chen and J. Naito, "A quantitative analysis of cells in the ganglion cell layer of the chick retina," Brain Behav. Evol. **53**(2), 75–86 (1999).
60. D. Troilo, M. Xiong, J. C. Crowley, and B. L. Finlay, "Factors controlling the dendritic arborization of retinal ganglion cells," Vis. Neurosci. **13**(04), 721–733 (1996).
61. A. J. Fischer and T. A. Reh, "Identification of a proliferating marginal zone of retinal progenitors in postnatal chickens," Dev. Biol. **220**(2), 197–210 (2000).
62. R. L. Binggeli and W. J. Paule, "The pigeon retina: quantitative aspects of the optic nerve and ganglion cell layer," J. Comp. Neurol. **137**(1), 1–18 (1969).
63. V. Budnik, J. Mpodozis, F. J. Varela, and H. R. Maturana, "Regional specialization of the quail retina: ganglion cell density and oil droplet distribution," Neurosci. Lett. **51**(1), 145–150 (1984).
64. R. N. Weinreb, A. W. Dreher, A. Coleman, H. Quigley, B. Shaw, and K. Reiter, "Histopathologic validation of Fourier-ellipsometry measurements of retinal nerve fiber layer thickness," Arch. Ophthalmol. **108**(4), 557–560 (1990).

1. Introduction

Chickens (*Gallus domesticus*) present several advantages as an animal model to study the mechanisms of myopia development [1]. For instance, they have large eyes that grow surprisingly fast (100 μm per day), exhibit good optics [2,3] and powerful accommodation [4]. Eye growth responds readily to alterations of visual experience, like treatments with lenses [5] or diffusers [6–8]. The chicken reaches maturity in less than a year [9]. Furthermore, it can be easily bred and maintained in the laboratory from the day of hatching. Chickens have also served as animal models for the study of the cornea wound healing after refractive surgery treatments, such as LASIK, LASEK or PRK [10–13].

The different ocular structures of the chicken (mainly the cornea and the retina) have been examined and imaged through several techniques such as electron microscopy [14], X-ray imaging [15], OCT [16] and fluorescence microscopy [17]. However, there is a lack of studies on the retinal cell densities at different eccentricities in chickens, using multiphoton imaging techniques. The development of femtosecond lasers as excitation sources allowed the development of multiphoton (or nonlinear) microscopy techniques, including two-photon excitation fluorescence (TPEF) and second-harmonic generation (SHG), which present high resolution and 3D imaging capabilities [18,19]. The basic principle underlying these techniques is that for tightly focused ultrashort laser pulses, the photon density is high enough to induce multiphoton absorption within the focal volume, providing intrinsic optical

3

sectioning. In addition, photobleaching and phototoxicity are significantly reduced, diminishing the damage within the sample. These non-destructive imaging methods exhibit the ability to section deeper within the samples, since the incident light lies in the infrared region of the spectrum. Furthermore, SHG does not deposit energy into the specimen due to its energy-conservation characteristics, providing minimal sample disturbance (e.g., thermal, mechanical side effects), which is desirable for biomedical studies.

In this work, the different parts of the chicken retina have been visualized with adaptive optics (AO) nonlinear imaging microscopy. The different morphological features and TPEF sources are also described. It is important to note that the nonlinear detected signal was exclusively due to endogenous fluorescence from the different molecules within the retinal structures, and staining procedures were not required.

2. Methods

2.1. Experimental setup and procedure

Details about the nonlinear microscope used in the present study can be found elsewhere [20,21]. The imaging system (Fig. 1) was developed on the basis of a modified inverted microscope and includes an AO module [22] composed of real-time Hartmann-Shack wavefront sensor (WFS150-5C, Thorlabs Inc., Newton, NJ) and a 140-actuator MEMS-type deformable mirror (Boston Micromachines, Cambridge, MA). The AO module was used to compensate for the laser beam aberrations in closed-loop.
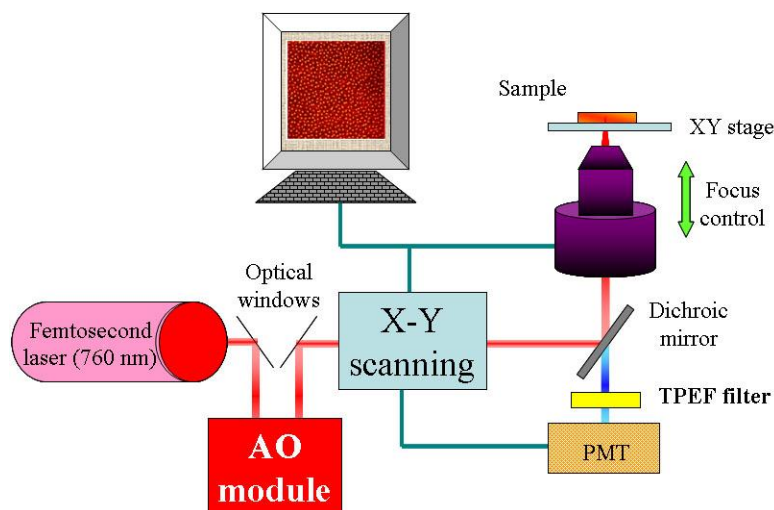

Fig. 1. Adaptive optics multiphoton microscope. AO module, adaptive optics module (Hartmann-Shack wavefront sensor and deformable mirror); PMT, photomultiplier tube.

A femtosecond Ti:sapphire laser (Mira900f, Coherent, St. Clara CA) was used as illumination and a pair of non-resonant galvanometric mirrors performed the X-Y image scanning. This laser system provided 110-fs pulses with a repetition rate of 76 MHz. Measurements were carried out with a wavelength of 760 nm. The laser beam reached the sample through the non-immersion long-working distance microscope objective (Nikon ELWD Series). Two microscope objectives were used (20x, NA = 0.5 and 100x, NA = 0.8) depending on the requirements of the experiment, concerning the magnification and resolution. The backward TPEF signal from the sample was collected through the same objective and a dichroic mirror was used to separate the excitation from the emission wavelength. This signal passed through a long-pass filter (TPEF filter, 435-700 nm), placed in front of a photomultiplier tube (PMT, Hamamatsu R7205-01, Japan) connected to a photon-counting unit. A DC-motor (focus control, PI C-136, Germany) was used to locate the focal plane along the Z axis, in order to acquire stacks of images for different depth positions. The

public domain image processing software "ImageJ" was used to reconstruct 3D images from the stacks of images. The entire experimental system was computer-controlled through a LabView[TM] custom-written software. The average intensity at the specimen plane ranged between 2 and 20 mW/cm^2, depending on the analyzed sample.

At each retinal location (i.e. eccentricity) series of six TPEF images were acquired at different depths (3-μm apart) throughout the retina (from the retinal nerve fiber layer to the outer segment). Each set of six individual frames were averaged to get a final image. To compute the density of photoreceptors and ganglion cells (GCs), an image contrast threshold was first applied and then the operator performed a manual counting operation. To determine the retinal eccentricities from the linear distances on the retinal surface, the values of posterior nodal distance (PND) and radius of the ocular globe of a schematic 30-day old chicken eye model were used [23]. Moreover, from each TPEF image corresponding to the photoreceptor mosaic the maximum potential anatomical resolving power (MARP, in cycles/deg) of the chicken eye was also computed as [24]

$$\text{MARP} = \frac{\text{PND}}{57.3 \cdot D_{\text{cone}} \cdot \sqrt{3}}, \qquad (1)$$

with PND being 6.2 mm [23] and D_{cone} the local average intercenter cone distance obtained as follows. For each photoreceptor mosaic image, the Fourier power spectrum was calculated, showing a ring due to the spatial distribution of photoreceptor, similar to that previously reported in other species retinas [25–27]. The parameter D_{cone} was directly related to the radius of the ring in the spatial frequency domain.

2.2. Samples

Five retinas from five adult chickens were analyzed. The samples were prepared at the Institute for Ophthalmic Research (Section of Neurobiology of the Eye) in Tubingen, Germany. All the study was carried out following the Guide for Care and Use of Laboratory Animals of the University of Tubingen. The animals were sacrificed with an overdose of ether anesthesia as previously described [28] and the ocular globes were excised. After cutting the globe in the horizontal plane behind the scleral ossicles, the vitreous was extracted and the retina, without RPE, was detached from the fundus and fixated with a paraformaldehyde solution (4%, in 0.1M phosphate buffer) overnight. The retinal tissue was flat mounted on a microscope slide and covered with a 130-μm thick cover slip. None of the samples was stained.

3. Results

Figure 2 shows a set of bright-field microscopy images of a chicken retina acquired at different depths. Due to the transparency of the retinal tissue in the visible part of the spectrum, this kind of microscopy does not provide images with sufficient contrast. Only in the photoreceptor layer, structures can be seen. These represent the oil droplets that are
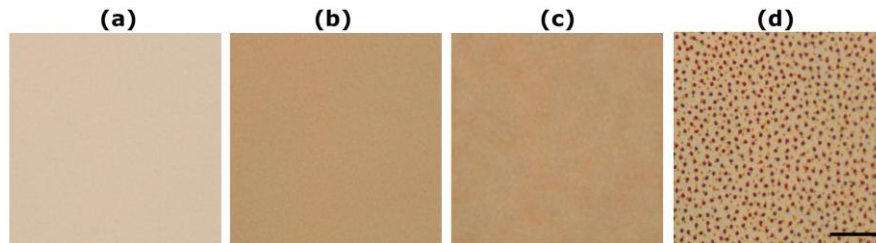

Fig. 2. Microscopy images of different chicken retinal layers acquired with a bright-field microscope and a 20x objective. Nerve fibers (a), ganglion cells (b), inner nuclear layer (c), and photoreceptors (oil droplets, see text) (d). Scale bar: 50 μm.
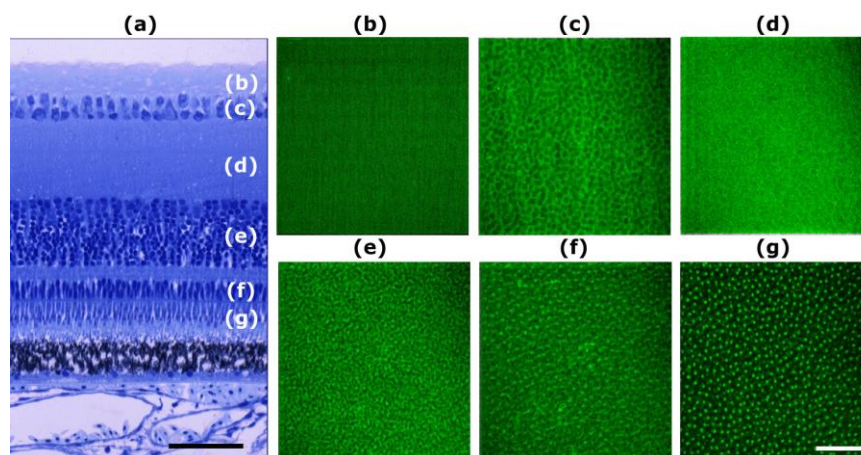
Fig. 3. (a) Histological transversal section of a fixed and stained chicken retina. (b)-(g) TPEF images of the different retinal layers acquired with a 20x objective: nerve fibers (b), ganglion cells (c), inner plexiform layer (d), inner nuclear layer (e), outer nuclear layer (f), and photoreceptors (oil droplets, see text) (g). Images correspond to a retinal eccentricity of about 30 deg. TPEF signal is exclusively due to the local endogenous fluorescence (autofluorescence). Scale bar: 50 μm.

located at the base of the inner segment above the outer segment [29]. These retinal cone oil droplets are heavily pigmented spherical organelles whose function is to filter the spectrum of light incident upon the visual pigment within the outer segment [30]. Since these structures permit the identification of individual cone photoreceptors, throughout this work we will use the term photoreceptor in a general sense when imaging the oil droplets.

A conventional plastic-embedded toluidine-stained transversal section of the chicken retina also acquired with a bright-field microscope is depicted in Fig. 3a. The different retinal layers, from the nerve fibers down to the photoreceptors can be discriminated. Below the photoreceptors, the retinal pigment epithelium and choroid are also seen. As an example, Figs. 3b-g present the TPEF microscopy (XY) images of different retinal layers acquired with the multiphoton microscope. TPEF clearly visualizes the retinal layers with a high spatial resolution. The corresponding retinal depth positions are labeled in Fig. 3a. Figure 3b shows the nerve fiber layer. The TPEF signal, originating from the underlying GC layer is clearly visible in Fig. 3c. Figure 3d depicts the weak TPEF signal from the inner plexiform layer. The endogenous fluorescence from the inner and outer nuclear layers is shown in Figs. 3e and 3f respectively. Finally, Fig. 3g shows the predominant TPEF signal from the photoreceptors.

For better visualization of the retinal structures seen under multiphoton microscopy, Fig. 4 exhibits another stack of TPEF images of the chicken retina acquired with a 100x objective. Similar to the previous figure, the retinal location of the imaged areas in Figs. 4b-g are marked in Fig. 4a. GCs are depicted in Fig. 4b. Figures 4c and 4d show the structure of the inner nuclear layer at two different depths (12 microns apart). This layer consists of amacrine cells and horizontal cells, respectively. Figure 4e depicts a different structure corresponding to the outer plexiform layer, mainly composed of synapses. Figure 4f illustrates the outer nuclear layer. Finally, Fig. 4g clearly exhibits the strong TPEF signal from the photoreceptors (bright discs).

Since stacks of individual frames along the Z direction were acquired, volume renderings of the whole retinal thickness can also be reconstructed. These representations provide valuable and detailed information of the retinal morphology. In particular Figs. 5a and 5b depict the same 3D tomography from two different viewpoints (top and bottom views respectively) for a stack of 33 images (optical sections) of the central retina. Figure 5c shows a diagonal cross-section obtained from Fig. 5a, where the different layers outlined previously
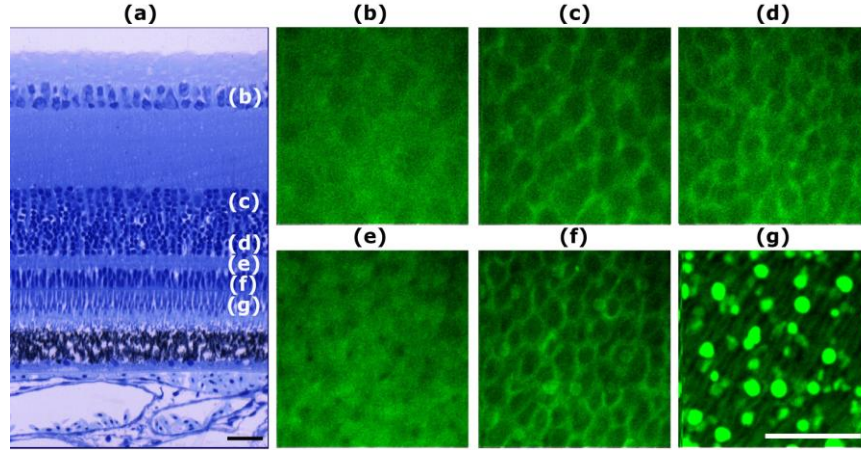
6

Fig. 4. TPEF in chicken retinal tissues. (a) The same transversal XZ section of a chicken retina as in Fig. 3a. (b)-(g) TPEF images acquired with a 100x objective for the same retinal area as in Fig. 3; (b) ganglion cells; (c and d) inner nuclear layer; (e) outer plexiform layer; (f) outer nuclear layer and (g) photoreceptors. Scale bar: 25 μm.
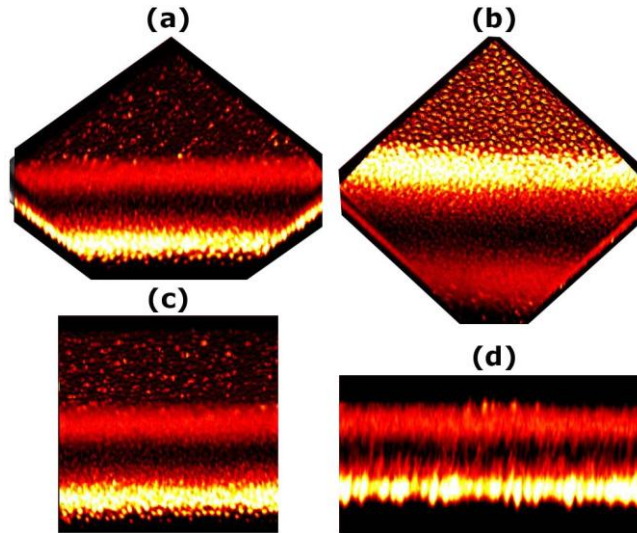
Fig. 5. (a, b) Reconstructed volume renderings of the chicken central retina: top (a) and bottom (b) views. Diagonal cross-section (c) and transversal tomography (d) computed from (a). A different false color has been chosen for a better visualization.

can be distinguished. Finally, Fig. 5d presents a transversal (XZ) section. It is evident that the maximum fluorescence signal comes from the photoreceptors layer. The dark area within the retinal structure corresponds to the inner plexiform layer, where fluorescence is almost negligible.

To evaluate the spatial distribution of both photoreceptors and GCs in the chicken retina, retinal areas at different eccentricities have been further examined. As an example, Fig. 6 shows the TPEF images corresponding to the GC layer and the photoreceptors for three different eccentricities (increasing towards the right). Due to the strong TPEF signal, the photoreceptors are clearly visible for each retinal eccentricity (Figs. 6d, 6e, and 6f). The density decreases when going towards the peripheral retina, being the highest at the central part (Fig. 6d).
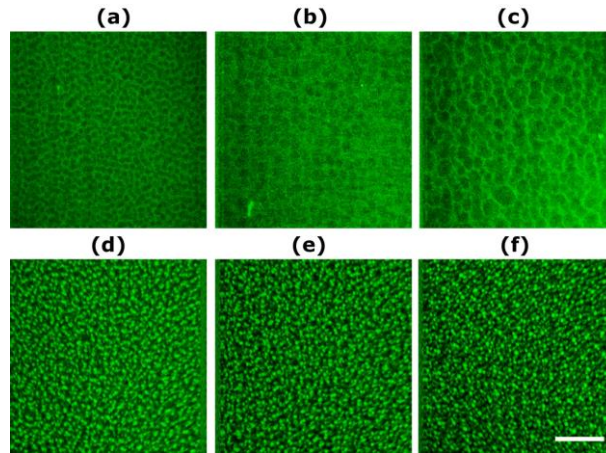
7

Fig. 6. TPEF images of the ganglion cells and photoreceptors of a chicken retina for different retinal eccentricities (12° (left), 50° (middle) and 85° (right). Ganglion cells (upper panels); photoreceptors (bottom panels). Scale bar: 50 μm.

At the central retina (left bottom panel) the density of photoreceptors for this particular sample was 20500 cells/mm^2. This density decreased down to 15500 and 11800 cells/mm^2 at the intermediate position (middle bottom panels) and the edge of the retina (right bottom panels) respectively. It should be noticed that these numbers are only indicative (see below), since only a limited number of samples was available. Figures 6a, 6b, and 6c correspond to the GC layer. Since these cells can be observed under multiphoton microscopy without using staining procedures, their density as a function of retinal eccentricity can also be computed. For these particular images the density values were about 10000, 8000 and 5000 cells/mm^2, which means that the number of GCs also reduces with retinal eccentricity. This reduction in density is accompanied by an increase in the GC size (this parameter has not been quantified in this work).

Figure 7 shows the density of photoreceptors for all specimens as a function of the retinal eccentricity. For these density values, a paired t-test showed a significant dependence with eccentricity (R = 0.86, p<0.0001). The fact that the highest density of photoreceptors is around the central part of the retina is well known and reported by others (see for instance [31]). Our results agree with these previous results. However, literature on exploring the morphology of the photoreceptors' mosaic and the distribution of GCs using nonlinear microscopy has not been found.
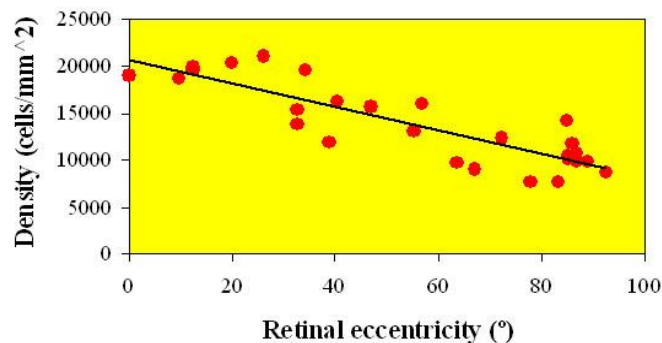

Fig. 7. Photoreceptor density values (cells/mm^2) as a function of retinal eccentricity. The black line fitted to the data gives a significant linear decrease with increasing retinal eccentricity (p< 0.0001). Linear fit: y = −175x + 20675.

8

The density of GCs also showed a significant decrease with retinal eccentricity (R = 0.85, p<0.0001; linear fit: y = −72x + 11457). For completeness, Fig. 8 shows the change in the density of both photoreceptors and GCs as a function of the retinal eccentricity grouped in intervals of 20 degrees. As expected, for both types of cells, the decrease was significant: R = 0.94, p = 0.006 for the former and R = 0.98, p = 0.003 for the latter.
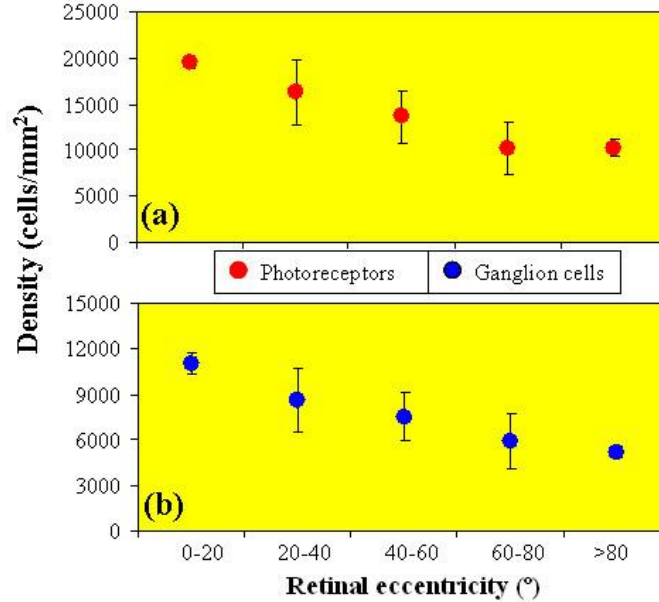

Fig. 8. Averaged density values (cells/mm^2) for photoreceptors (red symbols) and ganglion cells (blue symbols) as a function of retinal eccentricity.

From each TPEF image of photoreceptors, the MARP was computed as explained above. Figure 9 shows these values as a function of the retinal eccentricity. Results showed a significant decrease in the MARP with eccentricity (R = 0.76, p = 0.0001). For the sense of completeness, the image corresponding to the Fourier transform of a photoreceptor mosaic has also been included as an example.
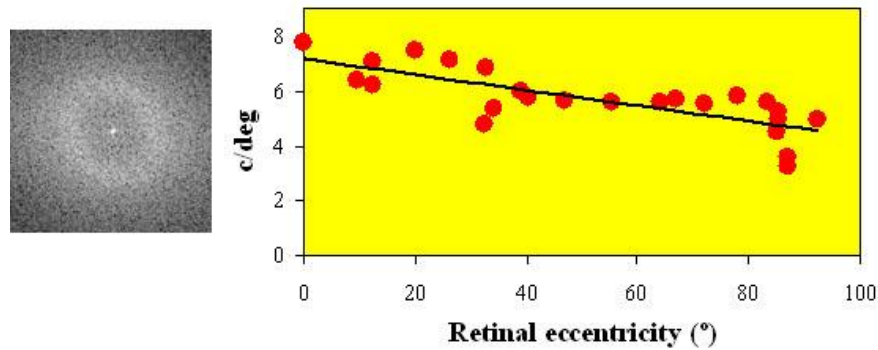

Fig. 9. Values of maximum anatomical resolving power (c/deg) in the chick retina as a function of retinal eccentricity computed using Eq. (1). An example of an image corresponding to the Fourier transform of a photoreceptor mosaic is shown on the left. Linear fit: y = −0.03x + 7.15.

4. Discussion

An AO multiphoton microscope has been used to visualize and characterize the structure of non-stained chicken retinas. The instrument provides TPEF images corresponding to different

9

retinal layers, from the retinal nerve fiber area to the photoreceptor mosaic. Moreover the quality of the images together with the intrinsic optical sectioning capabilities allows the 3-dimensional reconstruction of the retinal structures. These volume renderings might help to better visualize the areas of interest and to provide additional information on the spatial distribution of retinal cells.

The retina is a light sensitive and transparent tissue. Before striking the photoreceptors, the light passes through all neural layers. In standard experiments using bright-field microscopy for the analysis of retinal structures, different staining procedures and well-defined markers are used to isolate the signal from the different cells. These markers have particular responses to the different parts of the (broad-band) spectrum of the illumination source, what is essential for the visualization and identification of the features. The different retinal layers cannot effectively be imaged without these markers, as clearly shown in Fig. 2. In this sense multiphoton microscopy presents noticeable advantages. A unique wavelength is used to image the entire retina structure. Moreover, it is worth to take into account that the measured signal comes from the sample's autofluorescence (endogenous fluorescence) arising from specific molecules. This allows visualizing the different retinal cells without the need of histological markers.

To test if retinal cells provided SHG signal, the TPEF filter used in this work was changed by a narrow-band filter (380 ± 10 nm). Under this experimental condition no signal was detected, what confirms that autofluorescence is the only nonlinear signal provided by the retinal structures.

To our knowledge, this is the first time that TPEF images from the chicken retina are reported. Almost every retinal layer provides TPEF signal and although the different structures are lucidly distinguished, the photoreceptor oil droplets provided the strongest signal. Starting from the inner structure, the nerve fiber layer is observed. Although the origin of the signal from these fibers is not completely understood, they are also visible in ex-vivo human retinas [20]. Underlying this layer, the GCs were also detectable under nonlinear microscopy imaging. These cells are hardly visible with conventional microscopy unless staining substances are used. The autofluorescence signal from the GCs layer originates from the cytoplasm of the cells, while the dark part corresponds to the cell nucleus, which exhibits no signal (see for instance Fig. 3c). Two main sources are responsible for the endogenous fluorescence of the GCs: the mytochondrial oxidized flavin proteins, such as the yellow emitting flavin adenine dinucleotide (FAD) [32] and the mitochondrial reduced pyridine nucleotides NAD(P)H [33,34].

The inner plexiform layer provides a weak TPEF signal (Fig. 3d). For the inner nuclear layer the autofluorescence is located within the cytoplasm of amacrine and horizontal cells (see Figs. 4c and 4d). At the outer plexiform layer, mainly composed of synapses, the nonlinear signal is weakly observed (Fig. 4e). The cytoplasm of the cells within the outer nuclear layer was also easily observed (Figs. 3f and 4f). The photoreceptor mosaic was the area showing the strongest TPEF signal. The photoreceptors' inner segment (closer to the nuclear layer) contains organelles and the cells' nuclei. The nonlinear signal is due to mitochondrial NAD(H)P and FAD [35]. The outer segment (closer to the choroids) contains light-absorbing materials and the signal derives from all-*trans*-retinol, produced during the visual cycle.

Studies exploring the depth-resolved retinal structure using multiphoton microscopy are scarce in the literature. Some authors have shown TPEF images of the retinal pigment epithelium photoreceptor mosaic in humans [36,37] and mice [35,38]. TPEF images of GCs in porcine eyes [39] have also been displayed. Recently, we have studied the TPEF sources across the human retina, providing images of individual cells in a reliable and efficient manner [20,22]. We show the different layers of the chicken retina with enhanced contrast, imaged through backscattered TPEF microscopy without noticeable photodamage. An integrated morphological study can be performed as a function of both depth position and eccentricity, which elucidates the retinal structure. Due to the high resolution of the different retinal layers, it has been shown how the densities of photoreceptors and GCs change with

retinal eccentricity. Changes in the density of retinal cells with eccentricity are important since this parameter limits the ocular resolving power at different retinal locations. Moreover the knowledge of these densities might help to understand and quantify the loss of cells as a consequence of retinal pathologies and the development of ocular refractive errors.

Chicken (and birds in general) have among the most complex retinas of all vertebrates [40] and the analysis is difficult due to the extraordinary high density of small cells. Apart from rods and cones, the adult morphology of the chicken photoreceptor mosaic presents two types of cones and three types of double cones [41]. The counting procedure here performed included all types of photoreceptors and no distinction in terms of single or double-cones was made. For the samples here studied photoreceptor densities ranged from 20000 (area centralis) to 7700 cell/mm^2 (peripherally), with a mean of 13800 ± 4300 cones/mm^2. The highest density was located at the central retina and a gradual and significant decrease towards the periphery was present. This agrees with previous literature findings [31,42].

In general, mammals also show a decrease in the density of photoreceptors and ganglion cells towards the peripheral retina [43–47]. The peak density of photoreceptors was also found at the central retina for different birds, such as the duck [48] or the crow [49], although with densities well different: 33573 and 92109 cell/mm^2, respectively. A much lower density was found for the pigeon: 10021 cell/mm^2 [50]. Kram and associates [42] have recently reported that the density of cones in chickens decreases with increasing retinal eccentricity, although they did not provide data. They only provided numerical results on cone density at the mid-peripheral retina in four quadrants (17585 cones/mm^2 for all types of single cones). We found an average density of 15278 ± 1444 photoreceptors/mm^2 for areas between 40° and 60°, which is consistent with the previous result.

From the photoreceptor TPEF images we have computed the anatomical resolution as a function of the retinal eccentricity. We estimated the MARP to be between 6 and 7 c/deg at the central retina. This reduced to about 4 c/deg for the peripheral retina. Different authors have reported data on this parameter in birds. Values ranged between 140 c/deg for the eagle [24], 18 c/deg in pigeon [51], 6 c/deg for the quail [52] and about 4 c/deg in chicken [53]. This variability is also present when computing the behavioral spatial resolution in chicks, ranging between 1.5 c/deg reported by Over and Moore [54] and 6.0-8.6 c/deg measured by Schmid and Wildsoet [55], and Diedrich and Schaeffel [53]. Our estimates are similar to Ghim and Hodos' data [52] and higher than those reported by Diedrich and Schaeffel [53]. No data on MARP for different retinal eccentricities have been found in the literature to establish a comparison.

The density of GCs has been estimated in whole mounted retinas using different methods (see [56] for details). Changes in the distribution of GCs across the different parts of the chicken retina [57,58] were early reported. In particular, Ehrlich reported a reduction from 24000 (area centralis) to 4000 (edge) cells/mm^2 [57]. Later Chen and Naito estimated a decrease from 13500 to 4300 cells/mm^2 (average density: 8600 cells/mm^2) [59]. Other studies centered on the changes in GC density in the developing chick retina [60] or in the potential to generate new neurons [61]. A high-density region at the central retinal area was also found for aerial birds such as pigeons and quails [62,63]. Experiments in crows showed that the density of GCs diminished nearly concentrically from the central area towards the retinal periphery [49].

Unlike previous studies on chicken retinas, our multiphoton imaging technique was also able to visualize the GC layer with enough contrast to compute the density of cells without the need of histochemical markers. For our specimens the density of GCs ranged between 11400 (at the central retina) to 4000 cell/mm^2 (peripheral retina), with an average of 8100 cells/mm^2. The decrease with retinal eccentricity was also significant. These values agree with those estimated in [56]. In particular the information obtained with the present technique might be used to understand changes in visual quality and ratios among different types of retinal cells and analysis of generation and loss of retinal cells during development among others. Moreover, since the loss of GCs is directly involved in glaucoma development [64], their quantification might be useful to understand the origin and progress of this pathology.

In conclusion, it has been proven that multiphoton microscopy is a powerful tool to image the multilayered structure of retinal tissues in animal models (such as chicken presented herein) which provides complementary information. In particular, since the density of different retinal cells can be computed, changes in retinal organization can be tracked and comparisons between myopic and emmetropic eyes might be carried out. In that sense, the still-open question on whether the ocular enlargement with myopia leads to a stretching of the tissue or new cells are generated in order to maintain a constant density of cells (number per unit area), might be unveiled by using these nonlinear imaging techniques.

Acknowledgments